ROMANIAN ACADEMY
School of Advanced Studies of the Romanian Academy
Institute of Macromolecular Chemistry "Petru Poni"
CHEMISTRY Field

SUMMARY OF THE DOCTORAL THESIS

Multicomponent systems based on natural and synthetic polymers.

Synthesis, characterization, applications.

Ph.D SUPERVISOR:
Dr. Mariana PINTEALĂ

Ph.D:
Denisse-Iulia BOȘTIOG

2025

Romanian Academy
"Petru Poni" Institute of Macromolecular Chemistry

Mrs/Mr. .....

We inform you that on **31st of October 2025**, **12 am**, in the **"Petru Poni" Institute of Macromolecular Chemistry, Acad. Bogdan C. Simionescu**, Iasi, will take place the public presentation of the doctoral thesis *"Multicomponent systems based on natural and synthetic polymers. Synthesis, characterization, applications."*, by author **Denisse-Iulia Bostiog**, to confer the scientific title of doctor.

PRESIDENT:

CS I Dr. Marcela Mihai

"Petru Poni" Institute of Macromolecular Chemistry, Iasi

DOCTORAL SUPERVISOR:

CS I Dr. Mariana Pinteală

"Petru Poni" Institute of Macromolecular Chemistry, Iasi

REFEREES:

Prof. Univ. Dr. Lenuța Profire

Gr. T. Popa "University of Medicine and Pharmacy, Iasi

Prof. Dr. Valentin Năstase

"Ion Ionescu de la Brad" University of Life Sciences in Iași

CS I Dr. Habil. Luminita Marin

"Petru Poni" Institute of Macromolecular Chemistry, Iasi

In accordance with the Regulation on the organization and conduct of the doctorate for the granting of scientific titles in the Romanian Academy, we send you the summary of the doctoral thesis with the request to communicate your appreciations and observations. On this occasion, we invite you to participate in the public defense of your doctoral thesis.

Director,

Dr. Valeria Harabagiu

CONTENT

INTRODUCTION

Gold nanoparticles (AuNPs) were distinguished by their unique physicochemical properties, controllable size and shape, easily functionalized surface, high colloidal stability, and specific optical behavior (plasmonic effect) (Doctors *et al.*, 2021). These characteristics make them ideal candidates for targeted drug and gene delivery, as well as imaging applications (Chen *et al.*, 2016; Niu *et al.*, 2017; Ferreira *et al.*, 2020).

The theme choice of this doctoral thesis is motivated by the need to develop multifunctional, efficient, and safe systems for personalized antitumor therapies, capable of combining the capacity of tumor detection and localization with the targeted delivery of therapeutic loads. In particular, the interest is focused on the functionalization of AuNPs with biologically active molecules (peptides, cationic polymers, specific ligands), which confer selectivity and targeting to tumor cells, thus increasing therapeutic efficiency and reducing systemic toxicity.

In this doctoral thesis entitled "***Multicomponent systems based on natural and synthetic polymers. Synthesis, characterization, applications***", the aim was to obtain and optimize non-viral vector systems for the transport and release of genes and drugs, specific cell targeting, and SPECT/PET imaging.

In ***the first part*** of the doctoral thesis, **Chapter I**, a literature study based on the description of gold nanoparticles (AuNPs) is presented, which are widely considered to be superior delivery systems in medicine due to their ease of synthesis, surface functionalization, high stability, unique physicochemical properties, and biocompatibility.

The second part of the doctoral thesis is structured on four chapters (**Chapters II, III, IV, and V**) that present the personal contributions regarding the obtaining, optimization, and physicochemical characterization of non-viral vector systems based on gold nanoparticles, as well as the biological results obtained from *in vitro*, *in vivo* tests correlated with the results obtained *in silico*.

Within each chapter of the section on original results, the objectives of the investigation are presented, along with a discussion of the relevance of the approach to the proposed research theme, a detailed description of the experiments, the physico-chemical analyses, and the results obtained from biological and evaluations conducted *in vitro*, *in vivo*, and *in silico*. Additionally, each subchapter concludes with the specific conclusions drawn from the respective study.

Chapter II.1 presents the method of synthesis and in *vitro*, *in vivo,* and *in silico* evaluation of two non-viral vectors based on gold nanoparticles (AuNPs) functionalized with polyethylene glycol (PEG) of two different molecular weights that delimit polyethylene glycol (PEI) fragments, with the aim of better controlling the carrying capacity of DNA and drastically reducing toxicity. Peripheral functionalization with glucosamine residues enables the targeting of nanoparticles to biological environments with high glucose uptake. The vectors were characterized from a physicochemical perspective using UV-Vis spectroscopy, DLS, STEM, and FTIR. For quantitative evaluation, transfection efficiency was tested on HeLa cells, while cytotoxicity and biocompatibility were assessed using the CellTiter-Glo assay on both HeLa and HGF cell lines. Acute toxicity (LD_{50}) was evaluated via intravenous administration of AuNPs-PEG-PEG-PEI-PEG-GA and AuNPs-PEG-PEI-PEG-GA. Hematological and biochemical analyses, necropsy, and histopathological examinations were also performed. *In silico* studies were conducted to understand and predict the molecular level behavior of the non-viral vectors, providing additional information on their stability, size, and structural organization as a function of polymer composition.

Based on the results obtained in **Chapter II.1**, a non-viral vector with superior performance (AuNPs-PEG-PEG-PEI-PEG-GA) was highlighted in terms of complex efficiency, colloidal stability, and transfection capacity. Given these favorable characteristics, AuNPs-PEG-PEG-PEI-PEG-GA and AuNPs-PEG-PEG-PEI-PEG were selected for the exploration of advanced applications in the field of molecular imaging developed in **Chapter II.2**. Thus, they were subjected to the radiolabeling process with specific techniques using the radionuclides technetium-99m (^{99m}Tc) and gallium-68 (^{68}Ga), to evaluate their potential in SPECT and PET investigations. Instant thin-layer chromatography was used to evaluate the radiolabeling yield. The results obtained in the radiolabeling experiments were highlighted *in vivo* on an animal model. In this context, *in vivo* biodistribution studies represent an initial approach, demonstrating both the stability of the radiolabeled complexes in a biological environment and providing a means to monitor their pathway from administration to clearance.

In **Chapter III**, AuNPs with various methotrexate (MTX) functionalized coatings were developed to enhance antitumor activity, antioxidant properties, and biocompatibility. Stable phosphine-coated AuNPs were synthesized and subsequently functionalized with polyethylene glycol (PEG) and low-molecular-weight branched polyethylenimine (PEI800), followed by

covalent attachment of MTX. Physicochemical characterization was performed using UV-Vis, FTIR, DLS, STEM, and XPS spectroscopy. The antioxidant activity of the functionalized AuNPs was evaluated using the DPPH radical scavenging assay, as well as FRAP and CUPRAC assays. Biocompatibility and cytotoxicity were assessed through MTT and LDH assays on human HaCaT keratinocytes and CAL27 non-melanoma cancer cells.

Chapter IV presents the development of vectors based on functionalized AuNPs with polyethylenimine (PEI) and mono-tosylated β-cyclodextrin (CD), designed for the targeted delivery of genetic material. The synthetic strategy involved conjugating β-cyclodextrin with branched PEI of various molecular weights (800 Da, 2000 Da, and 25,000 Da), followed by the synthesis of AuPEInCD nanoparticles through the reduction of gold ions under microwave irradiation. In parallel, the Ad-PEG-Pep conjugate was prepared by reacting 1-adamantylamine with the PEG linker 12-SPDP, followed by coupling with a peptide (Pep) specific for MCF-7 cells. This conjugate was then used to form an inclusion complex with the β-cyclodextrin units on the nanoparticle surface, yielding the supramolecular final vector, AuPEInCD-Pep.

To confirm the structure of the intermediates and the final product, several characterization techniques were employed. NMR spectroscopy was used for the conjugated CD and CD-PEI products, while mass spectrometry (MS) confirmed the molecular weights of the Ad-PEG and Ad-PEG-Pep conjugates. FTIR spectroscopy revealed functional groups characteristic of PEInCD and AuPEInCD. Additionally, UV-Vis and TEM analyses were performed to assess the optical properties and morphology of AuPEI800CD, AuPEI2kCD, and AuPEI25kCD nanoparticles, as well as their peptide-functionalized variants.

Subsequently, the synthesized vectors were biologically evaluated through in vitro transfection and cytotoxicity assays on MCF-7, HGF, and HOS cells. Two strategies for peptide functionalization were compared: before or following polyplex formation with the pCS2+MT-Luc plasmid.

Chapter V provides a detailed account of the materials and methods used throughout the study, including synthesis procedures, physicochemical characterization techniques, and in vitro, in vivo, and in silico testing strategies.

CHAPTER II.1. Functionalized gold nanoparticles with biocompatible polymer and targeting molecules

The success of gene therapy largely depends on the efficiency and reliability of the molecular tools used for nucleic acid handling and delivery. In the present study, the synthesis and characterization methods were investigated, alongside the *in vitro, in vivo*, and *in silico* evaluation of two non-viral vectors, to improve the efficiency of genetic material delivery while minimizing potential adverse effects. Each system is based on gold nanoparticles (AuNPs) functionalized with PEG fragments of varying weights and PEI to better control DNA carrying capacity and reduce systemic toxicity. Peripheral functionalization with glucosamine further enables the nanoparticles to target biological environments with high glucose uptake, such as tumors.

II.1.2.2. Physicochemical characterization of functionalized gold nanoparticles

For both investigated structures, AuNPs-***PEG-PEG***-PEI-PEG-GA and AuNPs-***PEG***-PEI-PEG-GA, the overlapping spectra are shown in **Figure II.1.3.a**. The spectral regions corresponding to the hydroxyl and amine groups are highlighted around 3500 cm^{-1} νO-H and νN-H, along with νC-H present around 2800-3000 cm^{-1}. The stretch bond of the carbonyl is observed at about 1700 $cm^{-1,}$ and C-O is present at 750-1300 cm^{-1}.

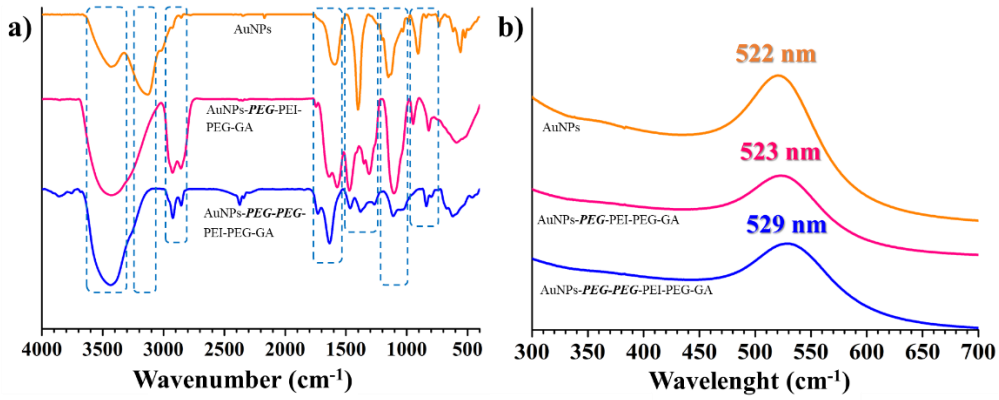

Figure II.1.3. (a) Overlapping IR spectra of AuNPs, AuNPs-***PEG-PEG***-PEI-PEG-GA, and AuNPs-***PEG***-PEI-PEG-GA; where: **1** –νO-H and νN-H; **2** – νO-H (carboxyl); **3** – νC-H; **4** – νC=O (carboxyl) and νC=O (carbonyl); **5** –νC-C and νN-H ; **6** –νC-O and νC-N; **7** –νC-H and νN-H. **(b)** Overlapping UV spectra of AuNPs, AuNPs-***PEG***-PEI-PEG-GA, and AuNPs-***PEG-PEG***-PEI-PEG-GA

All investigated nanoparticles exhibited a distinctive surface plasmonic resonance band (SPR) at approximately 520 nm (**Figure II.1.3.b**), indicating the presence of spherical nanoparticles.

The morphological characteristics of the nanoparticles were evaluated using STEM electron microscopy (**Figure II.1.6**).

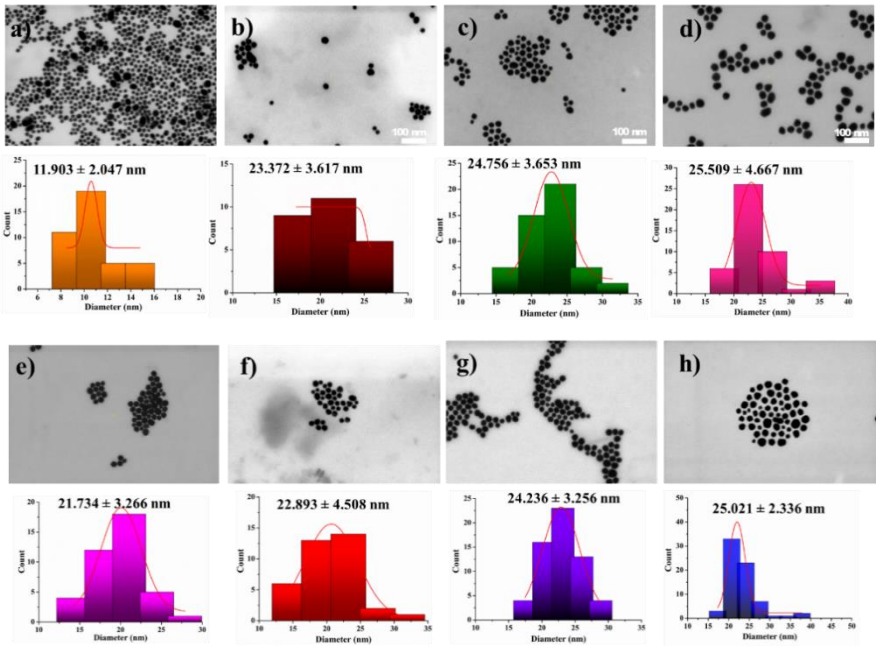

Figure II.1.6. STEM images and distribution of mean nanoparticle diameter throughout functionalization steps: **(a)** AuNPs; **(b)** AuNPs-PEG-epoxy; **(c)** AuNPs-PEG-PEI; **(d)** AuNP-***PEG***-PEI-PEG-GA; **(e)** AuNPs-PEG-NH_2; **(f)** AuNPs-PEG-PEG-epoxy; **(g)** AuNPs-PEG-PEG-PEI; **(h)** AuNPs-***PEG-PEG***-PEI-PEG-GA.

II.1.2.3. Interaction of vectors with DNA

Molecular modelling (MD) simulations (**Figure II.1.7.b** and **e**) demonstrate that in the absence of DNA, the PEI strands remain fully extended, forming a flexible 'crown' around the golden nucleus. This extension is determined by electrostatic repulsion between the positively charged cation groups ($-NH_2^+/-NH_3^+$) on the polymer chains. With the introduction of DNA (**Figure II.1.7.c** and **f**), a dramatic restructuring is observed: the PEI chains collapse, winding the DNA strand through electrostatic attractions between the positive groups of the PEI and the negative phosphate groups of the DNA. This structural transition not only highlights the key role of electrostatic interactions in the formation of vector-DNA complexes but also suggests a mechanism for optimizing DNA condensation, essential for transfection efficiency.

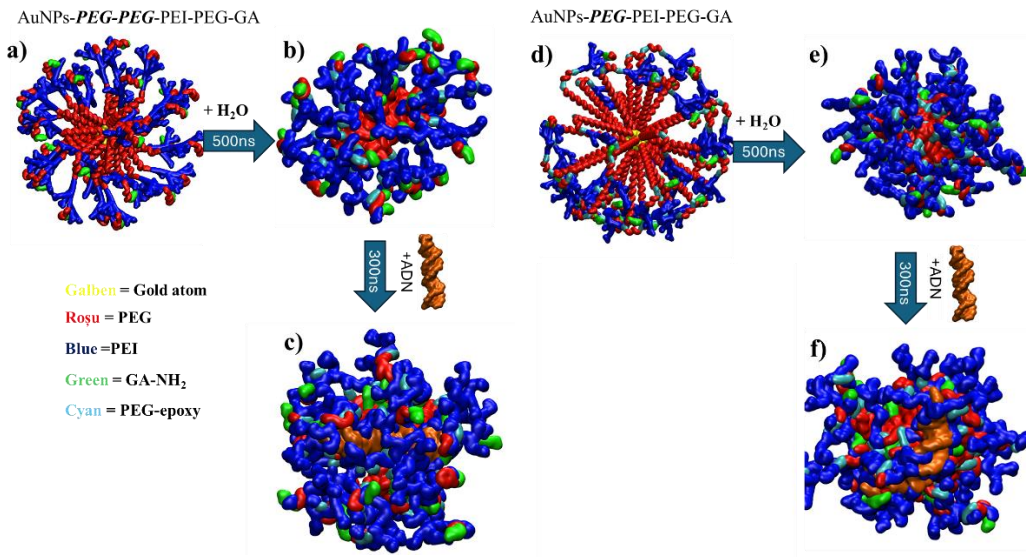

Figure II.1.7. Snapshots of the AuNPs-***PEG-PEG***-PEI-PEG-GA model **(a)** after construction, **(b)** after 500 ns balancing in water, and **(c)** after 300 ns simulation in the presence of a DNA fragment; Snapshots of the AuNPs-***PEG***-PEI-PEG-GA model **(d)** after construction, **(e)** after 500 ns balancing in water, and **(f)** after 300 ns simulation in the presence of a DNA fragment.

II.1.3.1. Plasmid DNA Condensation and Protection

The agarose gel electrophoresis assay was performed to evaluate the ability of AuNPs-***PEG-PEG***-PEI-PEG-GA and AuNPs-***PEG***-PEI-PEG-GA vectors to complex the pCS2+MT-Luc plasmid DNA, determining the binding efficiency at different N/P (nitrogen/phosphorus) ratios. The disappearance of free DNA bands and their complete retention in the complex indicates effective complexation, while the presence of migratory bands signals uncomplexed DNA.

The enzyme digestion test using DNase I (deoxyribonuclease I) was performed to evaluate the stability of DNA-vector complexes and the degree of protection offered by nanoparticles against enzymatic degradation.

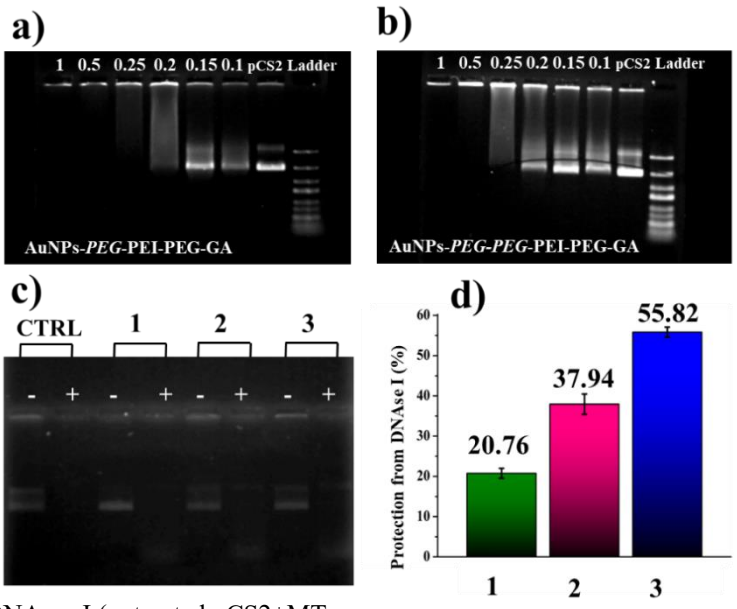

Figure II.1.7 Electrophoretic mobility of pCS2+MT-Luc in polyplexes consisting of **(a*)*** AuNPs-PEG-PEI-PEG-GA, **(b)**AuNPs-PEG-PEG-PEI-PEG-GA at different N/P ratios; **(c)** DNase I protection test, representative agarose electrophoresis of polyplexes with pCS2+MT-Luc incubated in the absence of (-) or in the presence of (+) DNase I, pCS2+MT-Luc as a control sample, **(1)** PEI, **(2)** AuNPs-***PEG***-PEI-PEG-GA and **(3)** AuNPs-***PEG-PEG***-PEI-PEG-GA; **(d)** Quantification of total bands with **(1)** PEI, **(2)** AuNPs-***PEG***-PEI-PEG-GA and **(3)** AuNPs-***PEG-PEG***-PEI-PEG-GA, after treatment with DNAase I (untreated pCS2+MT Luc value is equal to 100).

After incubation of DNAase I-treated polyplexes with SDS (**Figure II.1.6.d**), PEI, AuNPs-***PEG***-PEI-PEI-PEG-GA, and AuNPs-***PEG-PEG***-PEI-PEG-GA released 20.76%, 37.94% and 55.82% of the incubated plasmid DNA, respectively. Nevertheless, the AuNPs-***PEG-PEG***-PEI-PEG-GA vector retained the highest amount of DNA, followed by the vector with the shortest PEG chain length. Finally, the lowest DNA protection capacity was achieved in the case of PEI.

II.1.3.2 *In vitro* transfection efficiency

For qualitative evaluation, polyplexes were obtained by the interaction of PEI molecules with the pCS2+NLS-eGFP plasmid containing the gene to produce an enhanced green fluorescent protein (**Figure II.1.8**). It can be appreciated that, 48 hours after the treatment of HeLa cells with vector/DNA polyplexes, the transfection performed with the AuNPs-***PEG-PEG***-PEI-PEG-GA (**Figure II.1.8.a**) is stronger than that induced by the AuNPs-***PEG***-PEI-PEG-GA (**Figure II.1.8.b**). Both vectors are also able to transfect more efficiently than free PEI (**Figure II.1.8.c**).

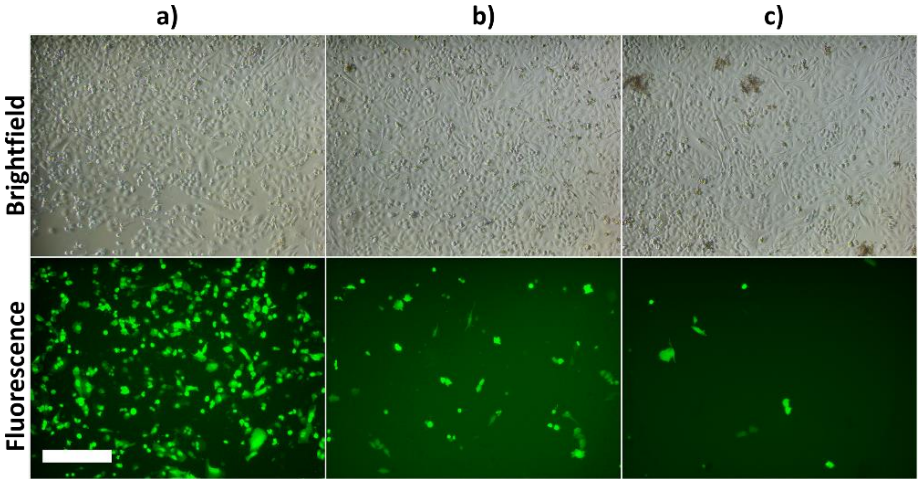

Figure II.1.8. Fluorescence microscopy of transfected HeLa cells. **(a)** AuNPs-***PEG-PEG***-PEI-PEG-G, **(b)** AuNPs-***PEG***-PEI-PEG-GA, **(c)** PEI. The cells were visualized under a microscope using the GFP filter, 48 hours after transfection. Scale: 200 µm.

This indicates that the length of the PEG chain plays a key role in achieving superior transfection performance.

II.1.4.5. Histopathological examination

Histopathological examinations were performed to investigate possible tissue damage induced by the administration of vectors (AuNPs-***PEG-PEG***-PEI-PEG-GA and AuNPs-***PEG***-PEI-PEG-GA). The primary objective of these analyses was to assess the effect of nanoparticles on the structure and morphology of the targeted organs, specifically the liver, spleen, kidneys, and lungs.

The presence of bi-nucleated cells indicates the existence of an ongoing regeneration process (**Figure II.1.13**). No other changes were observed, such as atrophy, congestion, changes in shape, volume, or color. Other organs, such as the lungs, kidneys, and spleen, were not affected and showed a normal appearance on histological sections.

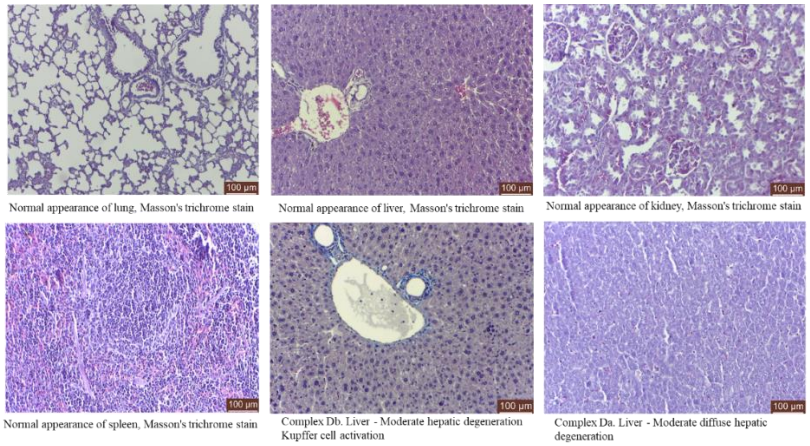

Figure II.1.13. Histological changes in the liver of BALB/c mice after administration of AuNPs-PEG-PEG-PEI-PEG-GA and AuNPs-PEG-PEI-PEG-GA vectors.

Histologically, no inflammatory changes were observed in the spleen, lungs, and kidneys. A slight hepatic degeneration, with activation of Kupffer cells, was recorded for both vectors, but the presence of bi-nucleated cells indicates a transient, reversible process that does not influence the health status of laboratory animals. Kupffer cell activation is responsible for early-stage damage to the liver, which is the main organ involved in the biotransformation of gold nanoparticles (Balasubramanian *et al.*, 2010).

CHAPTER II.2 Functionalized, radiolabeled gold nanoparticles as potential biocompatible agents for PET/SPECT techniques

Given the increasing incidence of cancer (Singh *et al.*, 2024), it becomes essential to develop effective treatments, as well as affordable and cost-effective methods for the early detection of this disease, a crucial factor in improving prognosis and survival rates. In this sense, nuclear medicine can establish a quick and accurate diagnosis. An essential condition in the application of the technique is the supply of radiolabeled substances suitable for the target tissue.

The present study explores the synthesis and characterization of functionalized vectors designed for SPECT and PET imaging. Their structure includes a gold core, a layer for radioisotope capture, a ligand for molecular recognition, and a polymer matrix designed to optimize biological interactions. Particular attention is also paid to decorating the envelope with GA units located in sterically impeded molecular environments, as selective accumulation of nanoparticles in areas with high glucose consumption is ensured.

II.2.2.3. Synthesis and characterisation of ^{99m}Tc and ^{68}Ga radiolabelled AuPEG-PEI and AuPEG-PEI-GA

To obtain the highest radiolabelling yield, the ^{99m}Tc procedure was performed with the variation of $Na^{+}{}^{99m}TcO_4^-$ activity (185 MBq/5 mCi), together with the nature and concentrations of $NaBH_4$ or $SnCl_2$ reducing agents. The formation of the complex between [$TcO4^-$] and the highly positively charged PEI was evidenced by a decrease in the zeta potential values observed 6 h after the radiolabeling process. The values decreased from +38 mV (baseline) to −38 mV for AuPEG-PEI/^{99m}Tc, from +3 mV to −60 mV for AuPEG-PEI-GA/^{99m}Tc, as shown in **Figure II.2.10.** At the same time, an increase in the zeta potential was observed after 22 hours, indicating +12.2 mV for AuPEG-PEI and +0.6 mV for AuPEG-PEI-GA.

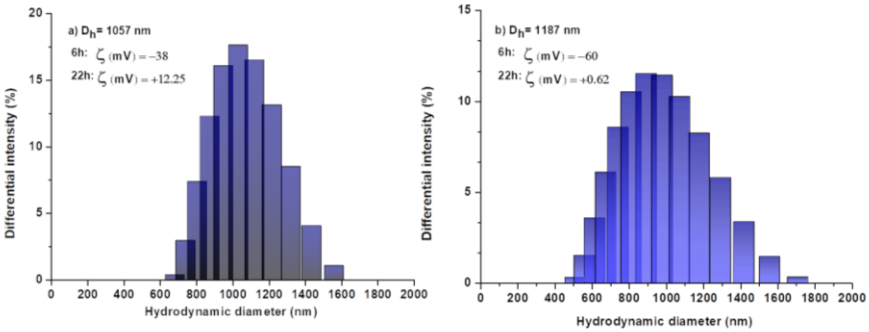

Figure II.2.10. Diameter and zeta potential values for **(a)** AuPEG-PEI and **(b)** AuPEG-PEI-GA after nanoparticle radiolabeling with ^{99m}Tc, using a 0.14 mg/mL $SnCl_2$ as a reducing agent. Zeta Potential Values **(g)** are shown in inserts (Uritu *et al.*, 2024).

The radiolabeling efficiency of AuPEG-PEI and AuPEG-PEI-GA reaches values of up to 99%, mainly during the initial 6-hour period, with minor variations based on the type and concentration of the reducing agent used. Data presented in **Figure II.2.12.c** indicates that the stability of the system is significantly affected by the presence of the reducing agent after a duration of 6 hours. The radiolabeling efficiency of the AuPEG-PEI-GA-^{99m}Tc complex was found to be 91% after 22 hours of incubation with $SnCl_2$ (0.14 mg/mL).

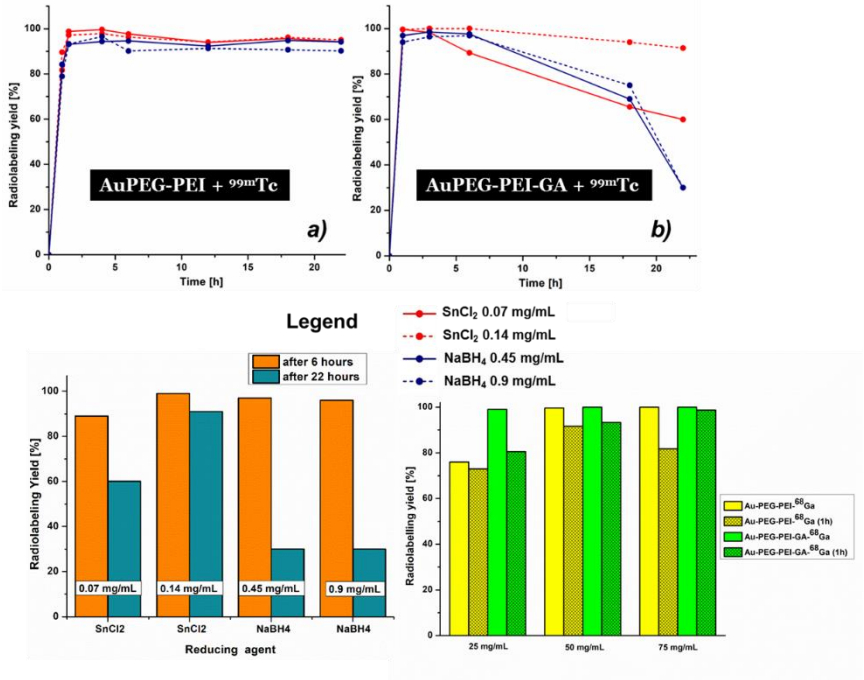

Figure II.2.12. Radiolabeling yield of nanoparticles **(a)** AuPEG-PEI and **(b)** AuPEG-PEI-GA cu ^{99m}Tc, performed with sodium pertechnetate with radioactivity of 185 MBq (5 mCi), corresponding to an N/^{99m}Tc of about 100/1; **(c)** The bar chart highlights the optimal conditions for AuPEG-PEI-GA radiolabeling; **(d)** Radiolabeling yields of AuPEG-PEI and AuPEG-PEI-GA with ^{68}Ga according to the ratio of nitrogen to gallium (N/Ga) (Uritu *et al.*, 2024).

The protocol applied for the ^{68}Ga radiolabeling process involved the use of a constant amount of $^{68}GaCl_3$ and three distinct concentrations of gold nanoparticles, which were combined to obtain N/Ga ratios of 50, 100, and 150. The coordination of $^{68}Ga^{3+}$ with the nitrogen present in the PEI coating led to the incorporation of the former into the PEI chains. Unlike complexes formed with $[^{99m}TcO4]^-$, $^{68}Ga^{3+}$ shows a preference for the formation of smaller entities.

Histograms generated from STEM images demonstrated that nanoparticle diameters fall within a narrow range of 22.12 to 23.6 nm, with negligible variations observed at different concentrations.

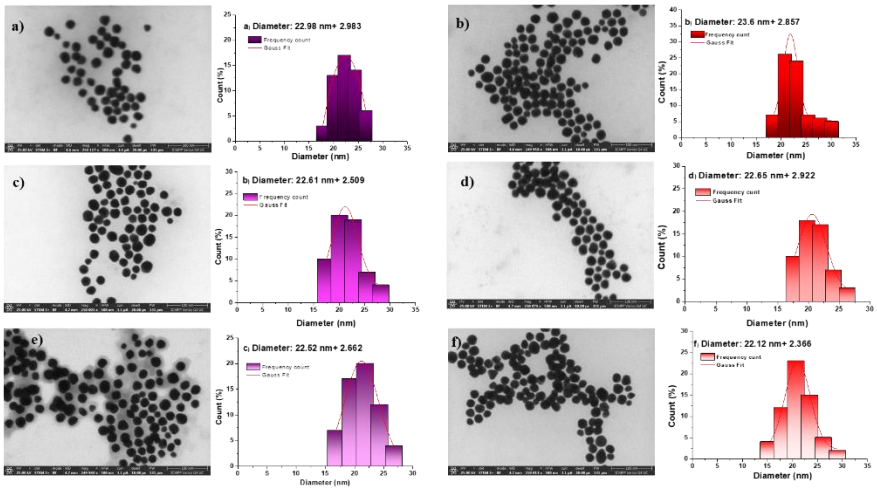

Figure II.2.13. STEM images of **(a,c,** and **e)** AuPEG-PEI/^{68}Ga and **(b,d,** and **f)** AuPEG-LIKE-GA/^{68}Ga to the selected N/Ga ratios: **(a,b)**, 50/1, **(c,d)** 100/ 1 and **(e,f)** 150 / 1. Histograms indicate dimensional distribution by measuring about 100 particles from multiple STEM images (Uritu *et al.*, 2024).

II.2.2.3 In *vitro* assay - effect of AuPEG-PEI and AuPEG-PEI-GA nanoconjugates before and after radiolabelling on normal human gingival fibroblasts

In *vitro* assay on fibroblasts (**Figure II.2.20.a**) demonstrated the biocompatibility of AuNPs, AuPEG-PEI, and AuPEG-PEI-GA at the tested concentrations, maintaining the cell viability over 70%. However, significant dose sensitivity was observed for AuPEG-PEI and AuPEG-PEI-GA, indicating the need for close monitoring of the concentrations used.

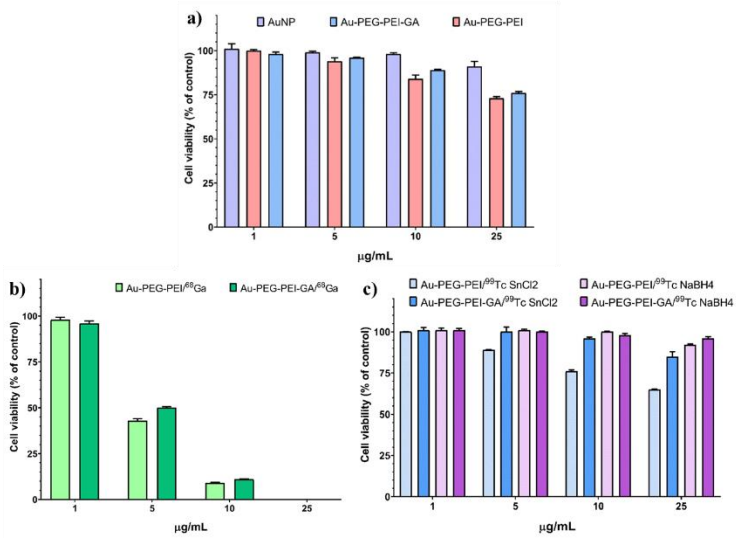

Figure II.2.20. Cytotoxicity Evaluation of Unlabeled and Radiolabeled Nanoparticles on Normal Fibroblasts at 24-Hour Incubation**: (a)** nanoparticle AuNPs, AuPEG-PEI, and AuPEG-PEI-GA; **(b)** AuPEG-PEI and AuPEG-PEI-GA marked with ^{68}Ga; **(c)** AuPEG-PEI and AuPEG-PEI-GA marked with ^{99m}Tc (Uritu *et al.*, 2024).

Radiolabeling with ^{68}Ga increased cytotoxicity even at low concentrations, suggesting that the optimal dose is 1 µg/mL to avoid a negative impact on fibroblast viability. In contrast, ^{99m}Tc labeling affected viability only at high concentrations, highlighting the variability of effects depending on the type of label and concentration.

II.2.2.4 *In vivo* biodistribution of radiolabelled AuPEG-PEI and AuPEG-PEI-GA nanoparticles

Figure II.2.21. illustrates the *in vivo* biodistribution of the AuPEG-PEI and AuPEG-PEI-GA systems radiolabeled with ^{68}Ga and ^{99m}Tc. The stability of both radiolabeled systems was tested and confirmed for up to 7 hours, with both showing favorable characteristics for use as radiotracers. Physiological thyroid uptake by the symporter NIS was present in (Franken et al.) ^{99m}Tc, but absent in AuPEG-PEI and AuPEG-PEI-GA.

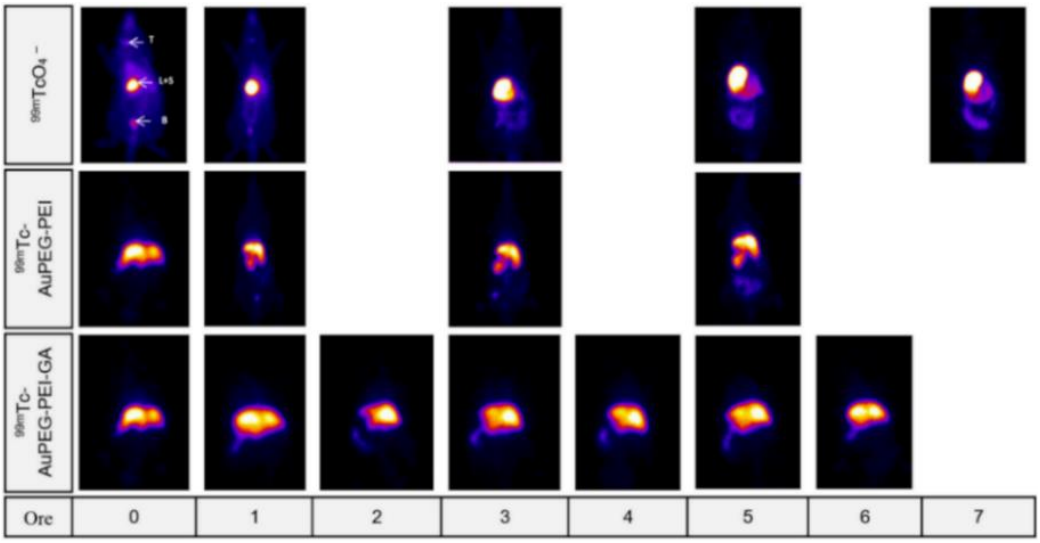

Figure II.2.21. Tissue absorption of radiolabelled nanoparticles ^{99m}Tc was investigated compared to the absorption of sodium pertechnetate. T = thyroid, St = stomach, B = bladder, L = liver, Sp = spleen, LK = left kidneys (Uritu *et al.*, 2024).

Analyzing **Figure II.2.22.** the free radionuclide (^{68}Ga) has a relatively nonspecific biodistribution, with a visible accumulation in several tissues such as the heart, brain, liver, stomach, and intestine. In the case of AuPEG-PEI/^{68}Ga, uptake is quite poor in most tissues, being more visible in the bladder and kidneys, therefore with a predisposition to rapid renal elimination.

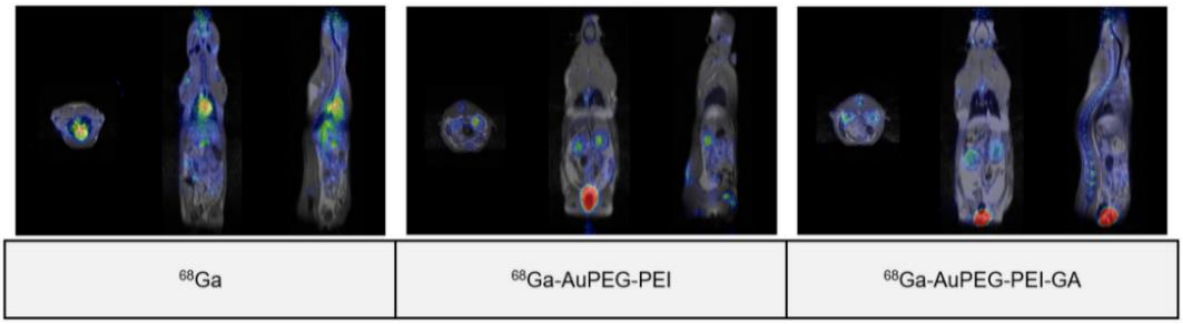

Figure II.2.22. Tissue absorption of radiolabeled nanoparticles ^{68}Ga compared to $^{68}GaCl_3$ freely highlighted by fused PET-MRI images (Uritu *et al.*, 2024).

The presence of GA in AuPEG-PEI-GA/^{68}Ga provides a biodistribution that highlights the compound without GA, which shows much better uptake in the nervous system (brain and spinal cord), and is also present in the kidneys and bladder. Preferential fixation in nerve tissue confirms the hypothesis that such a compound could be useful for imaging visualization of glucose-intensive tissues. This finding was confirmed only for radiolabeling with ^{68}Ga (PET), but not for ^{99m}Tc (SPECT), which reflects the fact that radiolabeling occurs through different mechanisms for the two radionuclides, making it possible to observe conformational changes that resulted in different biodistributions.

CHAPTER III - Methotrexate-functionalized gold nanoparticles: a novel nanotherapeutic approach for antitumor, antioxidant activity, and improved biocompatibility

Targeted drug delivery systems have the potential to enhance the therapeutic efficacy of drugs by increasing their accumulation in target tissues while improving the target-to-non-target tissue ratio (Qiu and DelVecchio Good, 2021). This will, in turn, lead to a reduction in the minimum effective dose of the drug and associated drug toxicity, as well as an improvement in therapeutic efficacy at equivalent plasma concentrations (Sudimack and Lee, 2000).

In this study, a new method was proposed to improve the efficacy (antitumor and antioxidant properties) and safety of methotrexate by using two distinct systems as gold nanoparticle-based nanocarriers (AuNPs) functionalized with PEG and PEI.

By binding MTX to polymer-functionalized AuNPs, it can accumulate better in tumor cells for a longer duration, leading to improved pharmacokinetic behavior and a stronger therapeutic effect.

III.2.1. Synthesis of two gold nanoparticle-based systems functionalised with methotrexate (AuNPs-PEG-NH_2-MTX and AuNPs-PEG-PEI-MTX)

The synthesis process (**Scheme III.1**) consisted of grafting SH-PEG-COOH onto the surface of phosphine-coated gold nanoparticles, and the second coating was created by coupling short-branched PEI fractions, followed by covalent binding of MTX, resulting in the AuNPs-PEG-PEI-MTX system. The second system (AuNPs-PEG-MTX) resulted from the functionalization of gold nanoparticles with SH-PEG-NH_2, followed by the covalent binding of methotrexate.

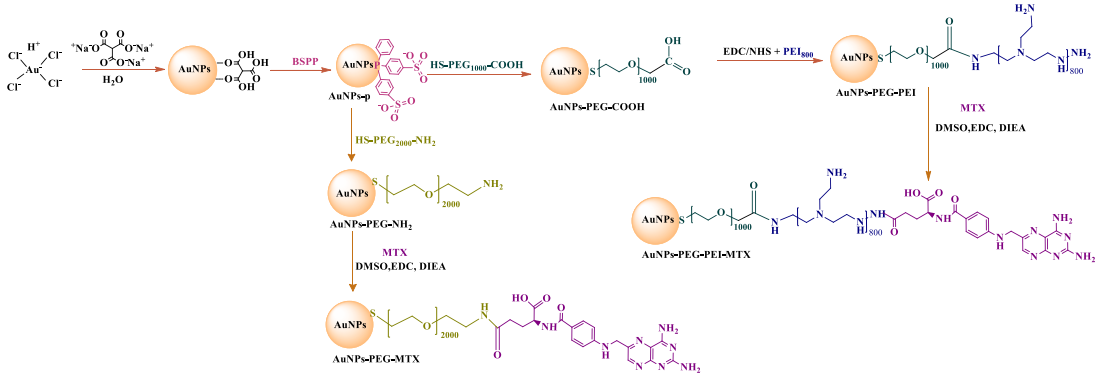

Schema III.1. The synthesis path for the development of functionalized gold nanoparticles (Bostiog *et al.*, 2024).

III.2.2. Physicochemical characterization of functionalized gold nanoparticles (AuNPs-PEG-NH_2-MTX and AuNPs-PEG-PEI-MTX)

Free MTX exhibited three characteristic UV-Vis absorption maxima at 258 nm, 303 nm, and 374 nm (**Figure III.1.a**). The MTX-specific peaks at 303 nm and 259 nm in the spectra of functionalized AuNPs (**Figure III.1.c**) confirm the binding of MTX to the surface of the polymers, as previously reported (Tran *et al.*, 2013). Using the MTX calibration curve in water (**Figure III.1.b**), the calculated concentrations of MTX in AuNPs were 0.67 mg MTX/mL in AuNPs-PEG-MTX and 0.385 mg MTX/mL in AuNPs-PEG-PEI-MTX.

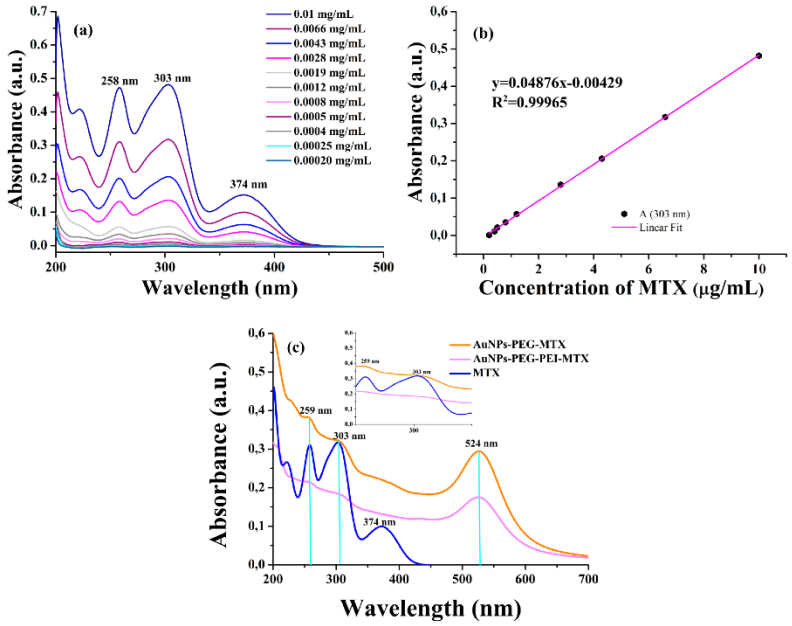

Figure III.1. The UV-Dream spectrum of the **(a)** MTX in water at different concentrations**, (b)** curba de calibrare a MTX**, (c)** spectrele UV-Vis ale MTX, AuNPs-PEG-MTX și AuNPs-PEG-PEI-MTX, **(d)** gold nanoparticles functionalized with polymers after each step (Bostiog *et al.*, 2024).

The formation of spherical morphology of MTX-functionalized and non-functionalized gold nanoparticles is further supported by the STEM technique (**Figure III.4**).

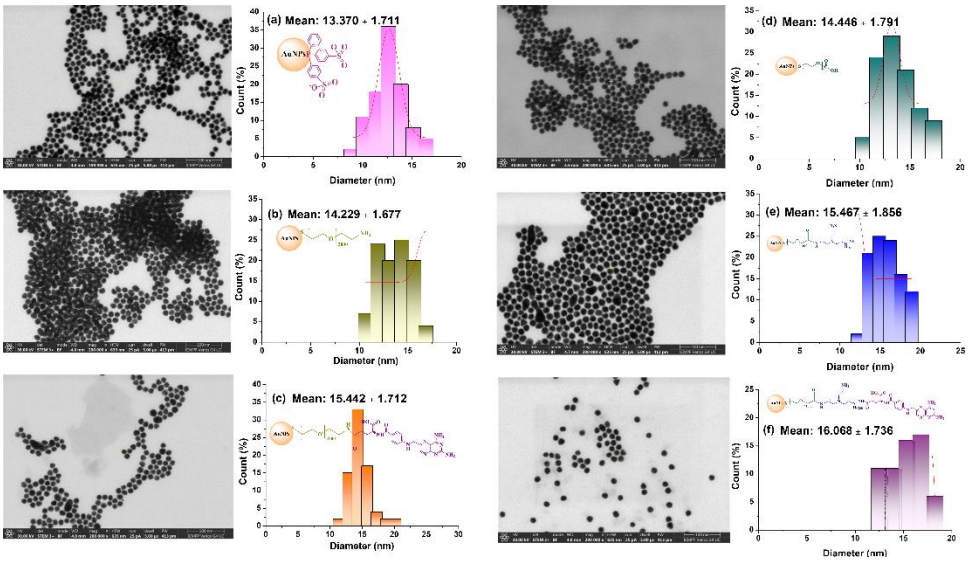

Figure III.4. Scan-transmitted electron microscopy images and histograms of the dimensional distribution of the nanoparticles investigated: **(a)** AuNPs-p, **(b)** AuNPs-PEG-NH_2, **(c)** AuNPs-PEG-MTX, **(d)** AuNPs-PEG-COOH, **(e)** AuNPs-PEG-PEI, **(f)** AuNPs-PEG-PEI-MTX (Bostiog *et al.*, 2024).

Nanoparticles have a low polydispersity and an average diameter of 13 ± 1.711 nm (AuNPs-p), 14 ± 1.677 nm (AuNPs-PEG-NH_2), 15 ± 1.712 nm (AuNPs-PEG-MTX), 14 ± 1.791 nm (AuNPs-PEG-COOH), 15 ± 1.856 nm (AuNPs-PEG-PEI), and 16 ± 1.736 nm (AuNPs-PEG-PEI-MTX). As anticipated, after surface functionalization, the nanoparticle sizes increase progressively at each step of functionalization.

III.2.3. Antioxidant activity

The antioxidant activity was determined both for AuNPs functionalized with MTX and for the intermediate products AuNPs-p, AuNPs-PEG-NH_2, and AuNPs-PEG-PEI, using the DPPH, FRAP, and CUPRAC methods.

AuNPs-PEG-MTX exhibit significantly higher antioxidant activity compared to AuNPs-PEG-PEI-NH_2, $p<0.0001$, for DPPH, CUPRAC, and free MTX tests at the same concentration as that found in nanoparticles, $p<0.0001$, for all three tests. These observations underscore the enhanced antioxidant potential achieved by MTX loading of AuNPs-PEG-NH_2 conjugates, outperforming both non-functionalized nanoparticles and free MTX. In contrast, AuNPs-PEG-PEI-MTX has significantly lower antioxidant activity compared to its precursor, as evidenced by the DPPH ($p<0.001$), FRAP ($p<0.0001$), and CUPRAC ($p<0.0001$) tests.

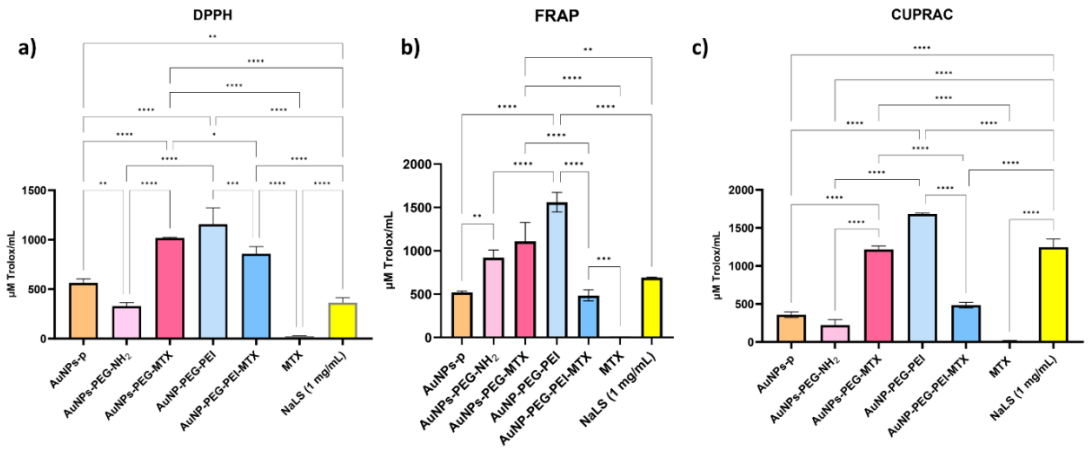

Figure III.7. Antioxidant activity of intermediates and functionalized nanoparticles: **(a)** DPPH, **(b)** FRAP, **(c)** CUPRAC (Bostiog *et al.*, 2024).

The DPPH method showed that AuNPs-p ($p<0.01$), AuNPs-PEG-MTX ($p<0.0001$), AuNPs-PEG-PEI ($p<0.0001$), and AuNPs-PEG-PEI-MTX ($p<0.0001$) had significantly higher antioxidant activity than the NaLS standard (**Figure III.7.a**). In the FRAP method, only the AuNPs-PEG-MTX ($p<0.01$) and AuNPs-PEG-PEI ($p<0.0001$) showed significantly higher antioxidant activity compared to the NaLS standard (**Figure III.7.b**). In the CUPRAC method, only AuNPs-PEG-PEI ($p<0.0001$) had higher activity compared to NaLS (**Figure III.7.c**).

III.2.4. Cytocompatibility of nanoparticles on dermal, normal, and tumor cell lines

Figure III.8 presents the results of the MTT assay evaluating the viability of the immortalized human keratinocyte cell line (HaCaT) and the squamous cell line CAL27. The data indicate that HaCaT cell viability was comparable to that of the control group, suggesting an absence of cytotoxicity. No statistically significant differences in viability were observed for the intermediate compounds, free MTX, or MTX-functionalized nanoparticles compared to the control.

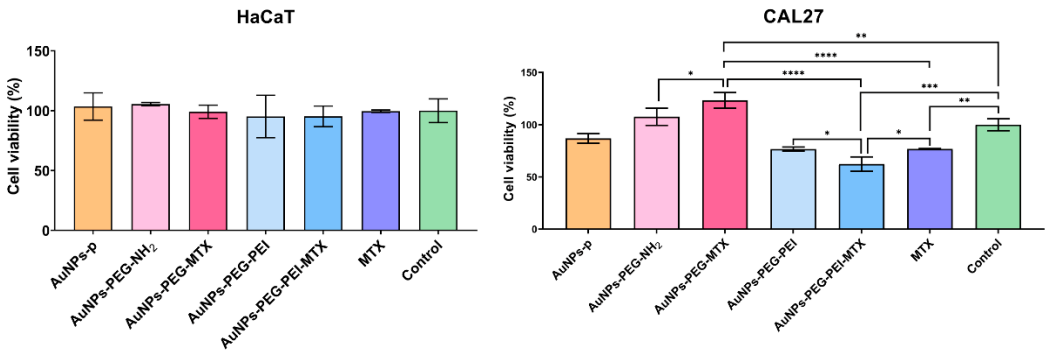

Figure III.8. Evaluation of the Biocompatibility of MTX-Functionalized Gold Nanoparticles by MTT Assay under Standard culture conditions of Human Keratinocyte Cell Line HaCaT (Left) and CAL27 Non-Melanoma Cancer Cell Line (Right) (Bostiog *et al.*, 2024).

In the case of tests performed on the CAL27 tumor cell line, different results were obtained, highlighting a reduction in cell viability that indicates the therapeutic potential of the studied compounds. AuNPs-PEG-PEI-MTX proved the best ability to decrease tumor cell viability, followed by free MTX and AuNPs-PEG-PEI.

The results of the Live/Dead test performed on each component of the systems (**Figure III.10)** corroborate the results of biochemical tests. Specifically, HaCat cells showed a significantly higher ratio of live cells (colored green) and dead cells (colored red) in **Figure III. 10. a**, which indicates an overall viability of HaCat cells in the presence of the tested conditions (Bhamidipati and Fabris, 2017). In contrast, tumor cells exhibited reduced viability in the presence of gold nanoparticles (**Figure III.10.b**), indicating that treatment with these nanoparticles exerts an antitumor effect (Uboldi *et al.*, 2009).

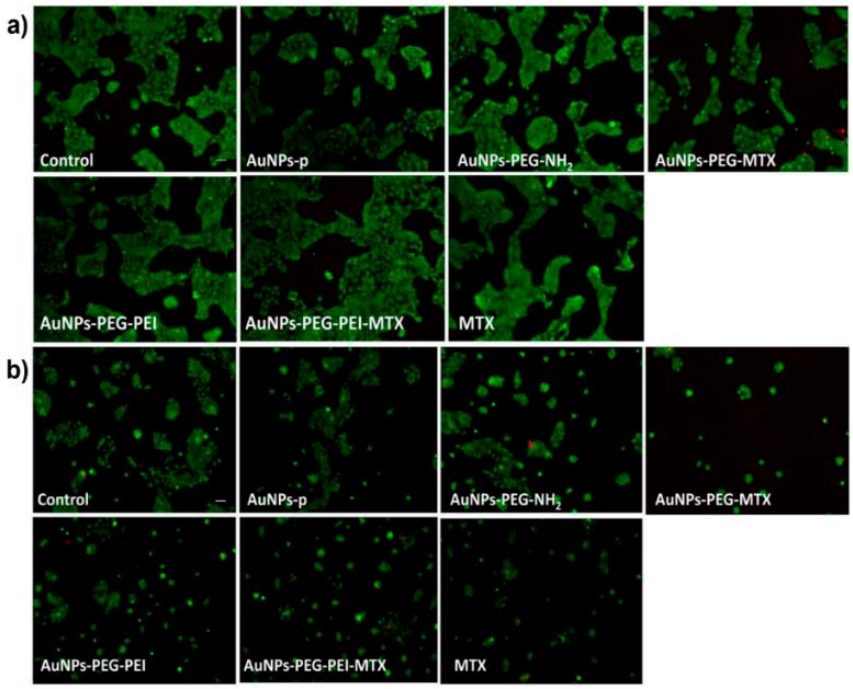

Figure III.10. Cell viability measured by Live/Dead test. **(a)** HaCat cells (normal) cultured for 24 hours in the presence of functionalized AuNPs; **(b)** Tumor cells (CAL27) cultured for 24 hours in the presence of functionalized AuNPs; scale – 100 μm (Bostiog *et al.*, 2024).

Cell viability tests showed that gold nanoparticles functionalized with MTX did not negatively affect healthy cells, demonstrating their potential as selective therapeutic agents for cancer cells. The nanoparticles were found to be biocompatible and showed low cytotoxicity on human HaCaT keratinocytes and on non-melanoma CAL27 cancer cells. These findings suggest that MTX-functionalized AuNPs hold promise for various biomedical applications, such as targeted cancer therapy and antioxidant-based treatments.

CHAPTER IV - Non-viral vectors of targeted delivery of genetic material

The modular system investigated in this study addresses several challenges in gene delivery, including targeting specificity, transfection efficiency, and minimal cytotoxicity. The vector design uses host-guest supramolecular chemistry between β-cyclodextrin and adamantan functionalized molecules to create a dynamic and interchangeable surface architecture on the surface of gold nanoparticles. In vector construction, three types of bPEI (800 Da, 2,000 Da, and 25,000 Da) were tested to evaluate how the molecular weight of bPEI influences particle size, surface charge, DNA binding capacity, and transfection efficiency. Subsequently, to investigate the influence of the peptide on the *in vitro* performance, two strategies were analyzed: AuPEInCD functionalization followed by peptide labeling either before the formation of polyplexes with pCS2+MT-Luc (DNA) or after this process, to determine the optimal moment of peptide introduction to maximize transfection efficiency.

IV.2.1. Synthesis of non-viral vectors

The experimental procedure for obtaining vectors based on gold nanoparticles was carried out according to **schemei IV.1**, following a synthesis pathway involving two main steps: the formation of gold nanoparticles (AuNPs) functionalized with a conjugate of polyethylenimine and β-cyclodextrin (PEInCD), and the preparation of a peptide-PEG derivative$_{12}$-SPDP-adamantan (Ad-PEG-Pep) which can form an inclusion complex with the β-CD units on the surface of the nanoparticles thus leading, in the final step, to the obtaining of supramolecular nanoparticles of AuPEInCD decorated with the peptide for specific cell targeting (Craciun *et al.*, 2023).

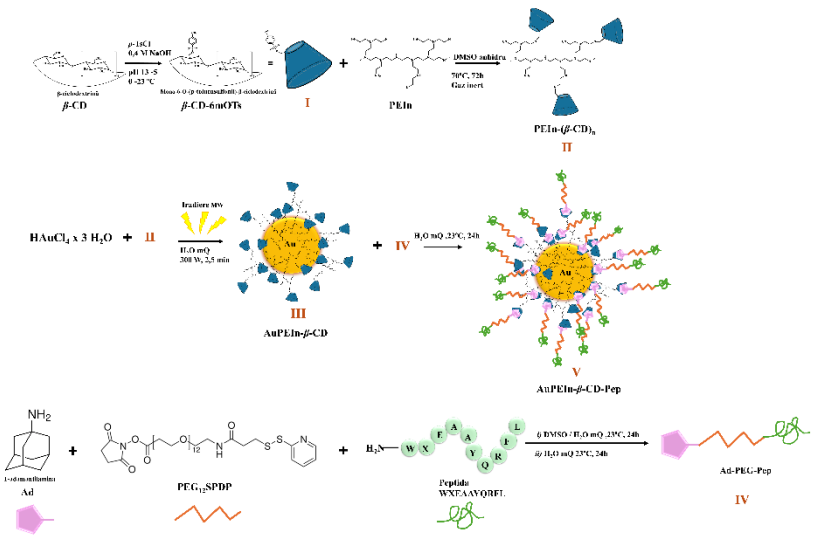

Diagram IV.1. Experimental Way to Obtain Non-Viral AuPEInCD-Pep Vectors (PEIn MW: 800 Da, 2,000 Da, and 25,000 Da).

IV.2.2. Characterization of non-viral vectors of targeted delivery of genetic material

To confirm the chemical changes suffered by β-CD following functionalization reactions, nuclear magnetic resonance spectroscopy (NMR) was used.

Compared to the well-known proton spectrum of β-CD (**Figure IV.1.a**), the introduction of the p-toluenesulfonyl group on a glucose subunit induces some changes in the NMR pattern of β-cyclodextrin (**Figure IV.1.b**). The remainder of the beta-cyclodextrin protons exhibit overlapping resonance signals in the range of 3.0-4.0 ppm, while protons from the hydroxyl group were assigned to the two signals at 4.50 (OH-6) and 5.73 ppm (OH-2 and OH-3). The presence of the p-toluenesulfonyl group is easily recognizable by the singlet at 2.44 ppm (CH_3) as well as the two doublets located in the region of the low magnetic field, characteristic of the protons in the aromatic nucleus, thus confirming the presence of the p-toluenesulfonyl group.

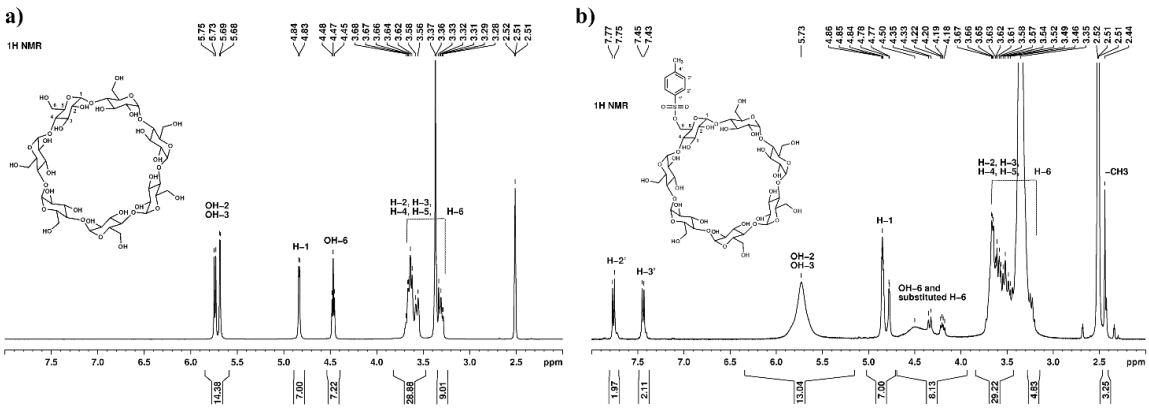

Figure IV.1. ^{1}H NMR spectra corresponding **to a)** β-CD and **b)** β-CD-Ts. Both spectra were recorded in DMSO-d at 400 MHz.

Electrospray ionization mass spectrometry (ESI-MS) was used to confirm the structure of the synthesized Ad-PEG-Pep compound.

The molecular ion peak for Ad-PEG12 was detected at m/z 948 [M+], corresponding to the calculated mass of 947. In addition, the spectra revealed the presence of an unreacted residual adamantyl fraction.

Similarly, Ad-PEG-Pep was identified at m/z 1353, aligning exactly with the expected molecular weight (m/2z), along with a secondary peak at m/3z 902 (**Figure IV.3**). In addition, residual Ad-PEG12 was detected at m/z 970, corresponding to sodium adduct (Ad-PEG+Na), indicating the presence of minor unreacted intermediates.

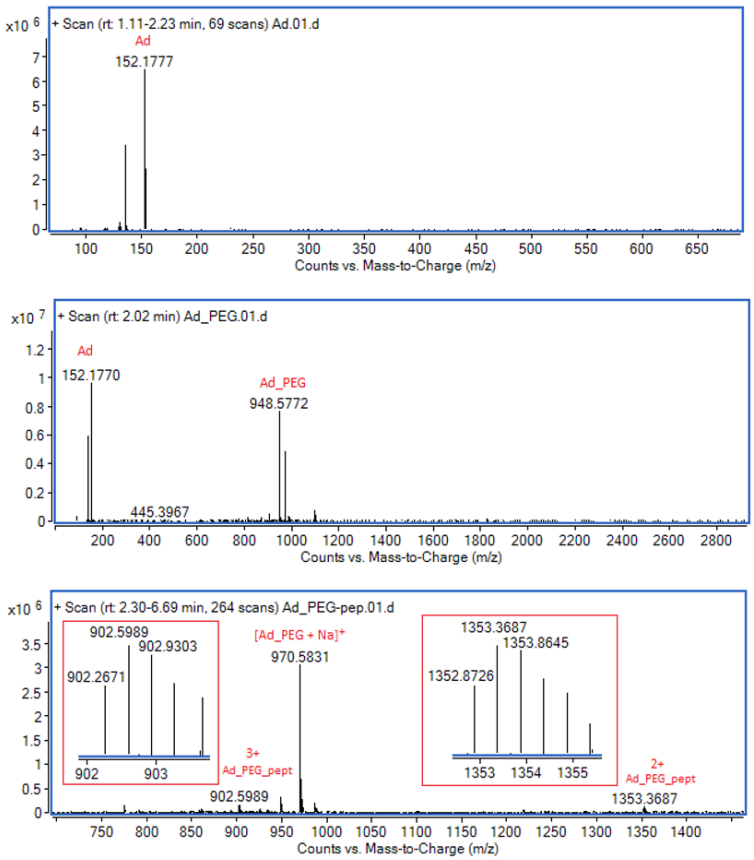

Figure IV.3. MS spectrum of Ad-PEG-Pep and intermediates.

IV.2.3. Characterization of AuPEInCD vectors in interaction with pCS2+MT-Luc

To evaluate the influence of the peptide on *in vitro* performance, two strategies were investigated: AuPEInCD functionalization followed by peptide labeling either before the formation of polyplexes with pCS2+MT-Luc (DNA) or after this process (**Scheme IV.2**).

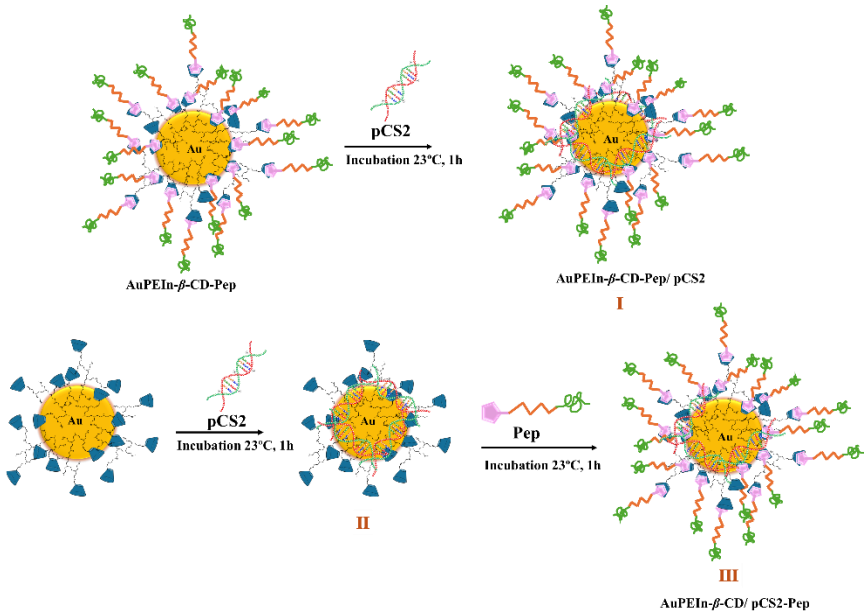

Diagram IV.2. Schematic representation of the preparation process for peptide-labeled non-viral AuPEIn-CD vectors before and after plasmid polyplex formation.

Transmission electron microscopy (TEM) was used to obtain detailed information on the morphology and size of the nanoparticles resulting from the formation of AuPEInCD/pCS2 polyplexes.

In the case of gold nanoparticles, studies have shown that particles with a larger diameter can carry more plasmid due to the surface area, but the density of DNA on the surface decreases as the particle size increases (Vasiliu *et al.*, 2021). When PEI is used to form plasmid complexes, the molecular weight of PEI (25000 Da) can lead to more substantial complexes compared to smaller PEI molecules. This effect is consistent with observations where the diameter decreases by 1 or 2 nanometers following the packing of the plasmid (**Figure IV.9**).

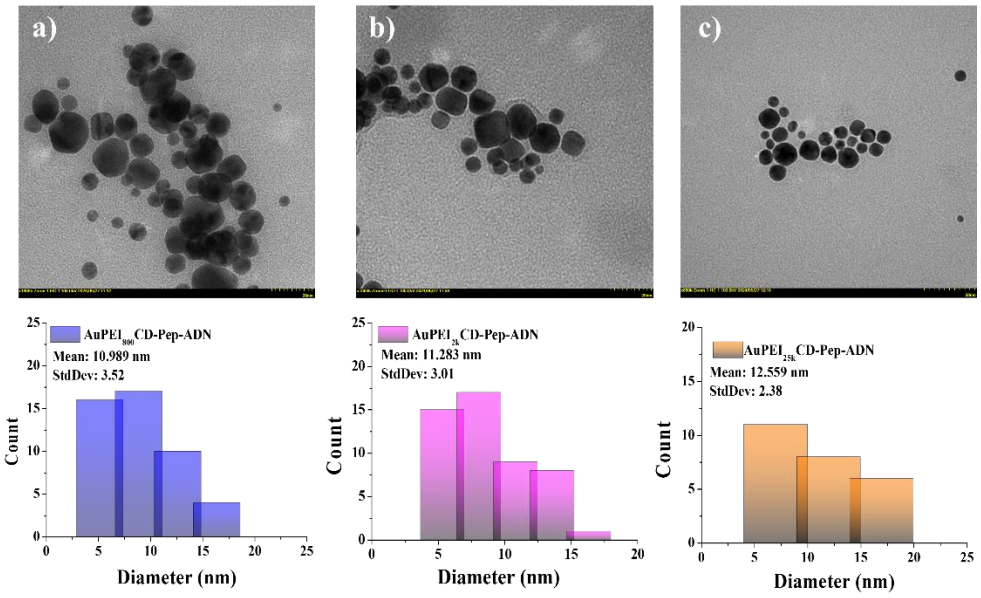

Figure IV.9. TEM images and their related size distributions for: **(a)** AuPEI800CD-Pep-DNA, **(b)** AuPEI2kCD-Pep-DNA, **(c)** AuPEI25kCD-Pep-DNA.

The enzyme digestion assay using DNase I (deoxyribonuclease I) was performed to evaluate the stability of non-viral vector polyplexes/DNA and the degree of protection offered by vectors against enzymatic DNA degradation. Two different approaches were used in the formation of polyplexes: in the first approach, Pep-labeled nanoparticles were complexed with plasmid DNA (AuPEIn-CD-Pep/pCS2), in the second approach, unlabeled nanoparticles (AuPEIn-CD) were complexed with plasmid DNA, followed by peptide labeling (AuPEIn-CD/pCS2+Pep). The comparison of these two types of complexes allowed the evaluation of the effectiveness of the vectors in protecting pCS2, an essential aspect for maintaining genetic integrity under biological conditions and for ensuring the success of transfection.

a.1=AuPEI$_{25k}$CD/pCS2/Pep-DNaza
a.2=AuPEI$_{25k}$CD/pCS2/Pep
a.3=AuPEI$_{2k}$CD/pCS2/Pep-DNaza
a.4=AuPEI$_{2k}$CD/pCS2/Pep
a.5=AuPEI$_{800}$CD/pCS2/Pep-DNaza
a.6=AuPEI$_{800}$CD/pCS2/Pep
a.7=pCS2 - Pep-DNaza
a.8=pCS2
L=Ladder

b.1=AuPEI$_{25k}$CD-Pep/pCS2 -DNaza
b.2=AuPEI$_{25k}$CD-Pep/pCS2
b.3=AuPEI$_{2k}$CD-Pep/pCS2 -DNaza
b.4=AuPEI$_{2k}$CD-Pep/pCS2
b.5=AuPEI$_{800}$CD-Pep/pCS2-DNaza
b.6=AuPEI$_{800}$CD-Pep/pCS2
b.7=pCS2 -DNaza
b.8=pCS2
L=Ladder

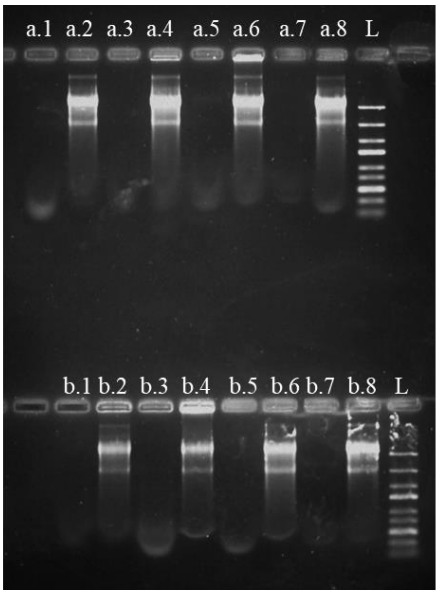

Figure IV.11. DNase I protection test, agarose representative electrophoresis of polyplexes with pCS2+MT-Luc, **(a)** AuPEInCD/pCS2/Pep and **(b)** AuPEInCD-Pep/pCS2 incubated in the absence or presence of DNase I, pCS2+MT-Luc as a control sample

The structural configuration of non-viral vectors plays a critical role in protecting therapeutic components (DNA, peptides) from enzymatic degradation. The study showed that the AuPEInCD/pCS2/Pep system protects pCS2 in a proportion of 25.66%, 23.94%, 25.5% in order of molecular weight increase, providing superior enzymatic protection compared to AuPEInCD-Pep/pCS2 (2.68%, 2.82%, 6.93% corresponding to increasing molecular weight), due to differences in molecular assembly and organization mechanisms (**Figure IV.12**).

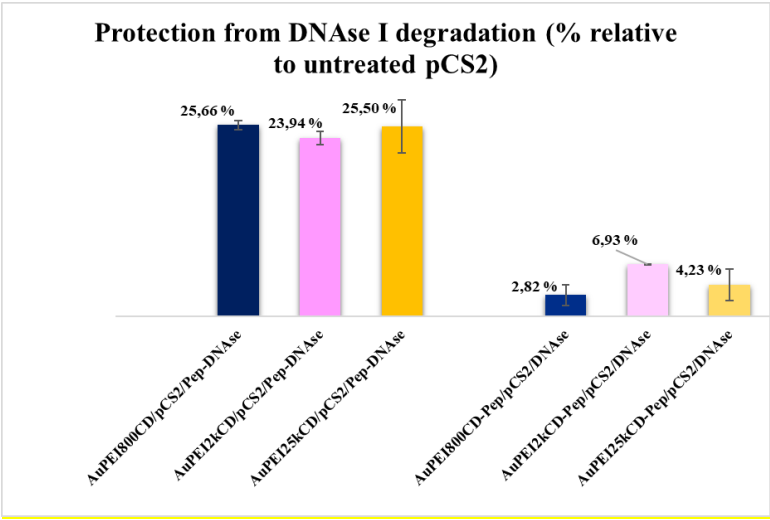

Figure IV.12. Quantification of the total electrophoretic bands of the unpacked and packaged plasmid for AuPEInCD/pCS2/Pep and AuPEInCD-Pep/pCS2 subjected to DNase I action.

IV.2.4. In *vitro* efficiency of non-viral vectors

Transfection efficiency was determined on HOS and MCF-7 cell lines, using pCS2+MT-Luc as the reporter gene (**Figure IV.13**). Two different approaches were used in the formation of the polyplex: Pep-labeled nanoparticles were complexed with plasmid DNA (AuPEIn-CD-Pep/pCS2), unlabeled nanoparticles were complexed with plasmid DNA, and then Pep labeling was performed (AuPEIn-CD/pCS2+Pep) (**Figure IV.13.a**).

Comparing the transfection efficiency in MCF-7 cells for the two experimental variants, we observed that the Pep labeling after polyplex formation resulted in better transfection compared to the classical approach.

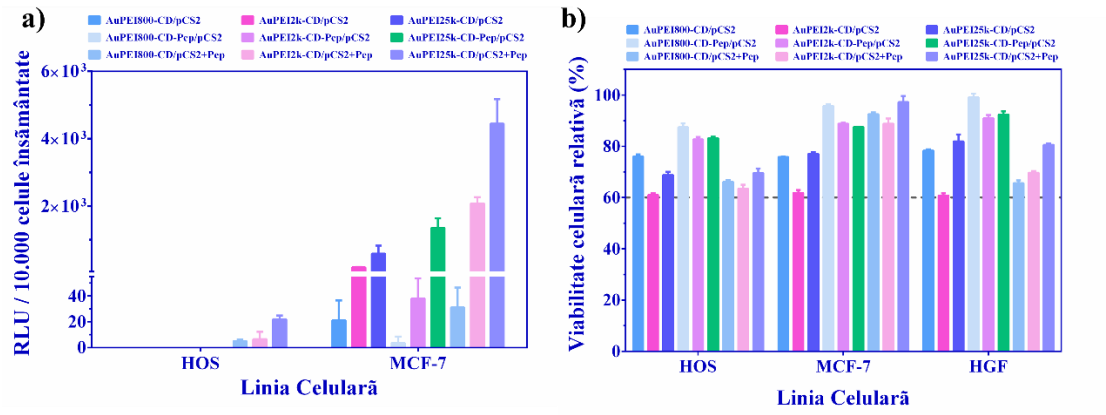

Figure IV.13. (a) Transfection efficiency in HOS and MCF-7 cells transfected with the pCS2+MT-Luc plasmid using polyplexes at an N/P ratio of 25**. (b)** Cell viability of HOS, MCF-7, and HGF cells treated with polyplexes at an N/P ratio of 25. Results are reported as % viability based on untreated control cells normalized to 100% and are expressed as mean value ± standard deviation (n=4).

Overall, cell viability exceeded 60% for all analyzed complexes, with peptide-labeled nanoparticles inducing lower cytotoxicity compared to their non-peptide-labeled counterparts (**Figure IV.11.b**).

The results suggest that the structure and composition of the vectors promote specific cellular internalization mechanisms in the target cells. In contrast, transfection efficiency was markedly lower in non-specific tumor cell lines, indicating selective vector targeting and the potential to minimize adverse effects in non-target cells.

GENERAL CONCLUSIONS

Personal contributions presented in the doctoral thesis **"Multicomponent systems based on natural and synthetic polymers. Synthesis, characterization, applications"** led to the following general conclusions for each chapter:

Chapter II.1

In this chapter, non-viral vectors of the types AuNPs-PEG-PEG-PEI-PEG-GA and AuNPs-PEG-PEI-PEG-GA were designed, synthesized, and characterized. These vectors are based on gold nanoparticles functionalized with polyethylene glycol (PEG), polyethylenimine (PEI), and glucosamine (GA).

UV-Vis spectroscopy confirmed the presence and stability of the nanoparticles through characteristic plasmon bands in the range of 522–529 nm, and their concentration was determined using the Lambert-Beer law. FTIR spectroscopy further validated the chemical functionalization by identifying bands specific to each component of the system.

Physicochemical characterization revealed hydrodynamic diameters of 369.6 nm and 386.8 nm, slightly different zeta potentials, and spherical morphology confirmed by STEM and TEM, with average sizes suitable for gene delivery applications. Molecular modeling corroborated the influence of polymer architecture on vector size, in agreement with experimental findings. Molecular modeling confirmed the influence of polymer architecture on the final vector sizes, in agreement with experimental observations.

The vectors' ability to protect and release DNA was evaluated through DNase I and SDS treatments, showing differential release rates. The extended polymer chain vector (AuNPs-PEG-PEG-PEI-PEG-GA) provided the best protection against enzymatic degradation, indicating a more compact and stable polyplex structure. This enhanced protection was reflected in transfection efficiency, as measured by the Bright-Glo assay, where the extended vector outperformed the simpler design in HeLa cell transfection.

Toxicological studies in animal models indicated low toxicity, with mean lethal dose (LD_{50}) values of 6 mg/mouse for the extended vector and 1.90 mg/mouse for the simplified vector, with no mortality or clinical signs of toxicity observed during the experiment. Hematological and biochemical parameters remained within physiological limits, with no significant alterations in liver or kidney function. The immune response was moderate, showing a slight and transient

increase in inflammatory cytokines (IL-6, TNF-α, IFN-γ) in the AuNPs-PEG-PEG-PEI-PEG-GA group, suggesting localized and controlled inflammation.

Histopathological analyses further supported the safety of the vectors, revealing physiological liver regeneration (presence of binucleated cells) without signs of degeneration, systemic inflammation, or morphological damage to internal organs (liver, kidneys, lungs, spleen).

Chapter II.2.

In this chapter, gold nanoparticle–based vectors functionalized with PEG, PEI, and glucosamine (GA), namely AuPEG-PEI and AuPEG-PEI-GA, were synthesized and subsequently radiolabeled with ^{99m}Tc and ^{68}Ga to evaluate their potential as molecular imaging agents and targeted delivery vectors. The chemical structures of the precursors were confirmed by ESI-MS, which revealed the specific molecular masses corresponding to the GA and PEG groups. The successful functionalization of the nanoparticles was further supported by FTIR and XPS analyses, which highlighted the presence of Au-S bonds as well as amino, carbonyl, and epoxy groups at successive stages of modification.

STEM morphological analysis revealed a progressive increase in nanoparticle size with each successive functional layer, from 11.9 nm for native AuNPs to 26.5 nm for the fully modified AuPEG-PEI-GA system. Complementary EDAX analysis confirmed the chemical composition, with the detection of key elements (Au, C, N, O, S) further supporting the successful stepwise functionalization.

Radiolabeling with ^{99m}Tc achieved high yields (>99% within the first 6 h) and demonstrated good stability over time, with only a slight decrease in efficiency observed after 22 h for the AuPEG-PEI-GA/^{99m}Tc system. Marked changes in ζ-potential following radiolabeling indicated a strong interaction between the radionuclide and the nanoparticle surface, affecting surface charge distribution and colloidal stability. Radiolabeling with ^{68}Ga was similarly efficient, yielding up to 100% labeling efficiency and exhibiting good stability as a function of the N/Ga ratio. Minimal variations in nanoparticle size further confirmed the structural integrity of the system under radiolabeling conditions.

FTIR spectroscopy of the radiolabeled compounds revealed structural modifications following labeling, most notably at the optimal N/Ga ratio of 100:1. Biocompatibility was evaluated *in vitro* on fibroblast, showing cell viability above 70% for the unlabeled vectors, thereby confirming their safety under the tested conditions. Radiolabeling with ^{68}Ga induced a slight increase in cytotoxicity at low concentrations, indicating that an optimal dose of 1 µg/mL is advisable to minimize adverse effects. In contrast, ^{99m}Tc labeling was better tolerated, with cytotoxic effects observed only at higher concentrations.

In vivo experiments demonstrated distinct biodistribution patterns between free radionuclides and vector-conjugated forms. Free ^{99m}Tc exhibited thyroid accumulation via the NIS transporter, whereas AuPEG-PEI and AuPEG-PEI-GA vectors did not display this uptake, suggesting a modified and more targeted biodistribution profile. For ^{68}Ga, the free radionuclide showed widespread nonspecific distribution across multiple organs, while the labeled vectors exhibited reduced nonspecific accumulation and predominantly renal clearance, highlighting favorable pharmacokinetics for non-invasive imaging applications.

Taken together, these results validate the AuPEG-PEI-GA platform as a multifunctional vector with strong potential for both SPECT and PET imaging. The system demonstrated chemical and colloidal stability, high radiolabeling efficiency, and satisfactory biocompatibility, supporting its translational relevance in molecular imaging.

Chapter III.

In this chapter, two nanostructured systems, AuNPs-PEG-MTX and AuNPs-PEG-PEI-MTX, were synthesized and systematically characterized following a stepwise functionalization strategy. Gold nanoparticles were first modified with PEG and PEI, followed by covalent conjugation with methotrexate (MTX).

UV–Vis spectroscopy confirmed the successful incorporation of MTX through the appearance of its characteristic absorption bands at 259 nm and 303 nm. Quantitative analysis revealed a higher drug loading efficiency for the AuNPs-PEG-MTX formulation compared to the PEI-containing system. FTIR spectroscopy further validated the conjugates by identifying the overlapping characteristic bands attributable to each component.

Dimensional analysis indicated small average particle sizes with low polydispersity, consistent with a uniform nanoparticle distribution. High-resolution XPS analysis confirmed the

coexistence of Au(0) and Au(I) oxidation states across all systems, supporting both the stability and the chemical integrity of the conjugates.

The evaluation of antioxidant capacity indicated that AuNPs-PEG-MTX exhibited superior activity compared to all other formulations, including the reference standard (NaLS), as determined by the DPPH, FRAP, and CUPRAC assays. This result suggests a synergistic role of PEG and MTX in enhancing the antioxidant activity of gold nanoparticles.

In vitro studies on healthy human cells (HaCaT) demonstrated good biocompatibility, with no notable cytotoxic effects observed for either the intermediate compounds or the final nanoparticles. Tests performed on the CAL27 cancer cell line showed a significant reduction in cell viability, which was most pronounced for the AuNPs-PEG-PEI-MTX formulation, followed by free MTX and the AuNPs-PEG-PEI system. These findings suggest enhanced antitumor efficacy when methotrexate is conjugated onto a nanostructured support.

The Live/Dead assay further supported these observations, indicating a favorable ratio of viable cells in the HaCaT culture, in contrast to the increased cell mortality observed in the CAL27 culture. This reinforces the hypothesis of selective cytotoxicity and potential therapeutic efficacy of the system.

Overall, these results demonstrate that gold nanoparticles functionalized with PEG, PEI, and MTX possess colloidal stability, enhanced antioxidant activity, good biocompatibility, and significant antitumor therapeutic potential.

Chapter IV.

In this study, six non-viral vectors based on gold nanoparticles, cyclodextrin (CD), and peptide-modified polyethylenimine were synthesized and characterized: AuPEI800CD, AuPEI2kCD, AuPEI25kCD, and their peptide-functionalized counterparts (AuPEI800CD-Pep, AuPEI2kCD-Pep, AuPEI25kCD-Pep). These vectors were designed for the efficient and selective delivery of the pCS2 plasmid.

The chemical functionalization was confirmed by MRI and FTIR spectroscopy, which demonstrated the successful attachment of CD to the PEI backbone, as well as specific changes in the functional groups involved. MRI data revealed that the degree of CD substitution depended on the molecular weight of PEI, with a higher substitution density observed for PEI25k (12 CD/molecule) compared to lower values for PEI800 and PEI2k (1CD/molecule). Mass

spectrometry confirmed the expected structure of the peptide (Ad-PEG-Pep), validating the success of the intermediate synthesis steps.

The physicochemical changes of the nanoparticles following functionalization were evidenced by a shift of the plasmon band in the UV-Vis spectra from ~520 nm to ~530 nm, indicating surface reorganization after peptide grafting.

Hydrodynamic size measurements and TEM analyses showed that nanoparticle size increased with the molecular weight of PEI and the addition of the peptide, while maintaining a regular spherical morphology. Packaging with the pCS2 plasmid resulted in significant size compaction, suggesting efficient interactions between components.

Agarose gel electrophoresis was crucial for determining the optimal N/P ratios for complete pCS2 binding, which varied depending on the vector structure. The most efficient ratios were observed for PEI25k, particularly in post-functionalized peptide combinations.

Regarding DNA protection, systems in which the peptide was added after the formation of the AuPEInCD/pCS2 complex (rather than prior) provided superior protection (23–26%), suggesting more efficient molecular organization and a better barrier against degrading agents.

Cell viability assessments on the HaCaT line showed viability greater than 60%. Cytotoxicity studies on HGF and HOS cell lines revealed that peptide-labeled vectors exhibited higher toxicity after complexation compared to those functionalized beforehand, indicating a direct influence of spatial organization on biological behavior.

In terms of transfection efficiency, the results showed a direct correlation between the molecular weight of PEI and the delivery capacity of pCS2, with the AuPEI25kCD/pCS2+Pep system achieving the highest performance, followed by the PEI2k and PEI800 versions. These findings suggest that higher PEI molecular weight contributes to both increased DNA compaction and more efficient cellular interaction.

In conclusion, the developed vectors exhibit promising structural, biochemical, and functional properties. Moreover, their molecular organization, particularly the sequence of functionalization steps, significantly influences both delivery efficiency and biological selectivity.

DISSEMINATION OF RESULTS

Articles published in ISI-indexed scientific journals, the results of which made the content of the doctoral thesis:

1. Craciun BF, Clima L, **Bostiog DI**, Silion M, Calin M, Peptanariu D, Pinteala M. Multilayer gold nanoparticles as non-viral vectors for targeting MCF-7 cancer cells. *Biomaterials Advances*. **2023** Jan 1;144:213201. (**IF = 5,5, Q1**);
2. **Bostiog DI,** Simionescu N, Coroaba A, Marinas IC, Chifiriuc MC, Gradisteanu Pircalabioru G, Maier SS, Pinteala M. Multi-shell gold nanoparticles functionalized with methotrexate: a novel nanotherapeutic approach for improved antitumoral and antioxidant activity and enhanced biocompatibility. *Drug Delivery*. **2024**, 31(1):2388624. (**IF = 6,5, Q1**).
3. Uritu CM, Al-Matarneh CM, **Bostiog DI**, Coroaba A, Ghizdovat V, Filipiuc SI, Simionescu N, Stefanescu C, Jalloul W, Nastasa V, Tamba BI. Radiolabeled multi-layered coated gold nanoparticles as potential biocompatible PET/SPECT tracers. *Journal of Materials Chemistry B*. **2024;**12(15):3659-75. (**IF = 6,1, Q1**);

Articles published in ISI-indexed scientific journals, whose results were related to the topic of the doctoral thesis (these results were not included in the thesis content):

1. Bouchekhou Z, Hadj Ziane-Zafour A, Lupascu FG, Profire BȘ, Nicolescu A, **Bostiog DI,** Doroftei F, Dascalu IA, Varganici CD, Pinteala M, Profire L. Binary and Ternary Inclusion Complexes of Niflumic Acid: Synthesis, Characterization, and Dissolution Profile. *Pharmaceutics*. **2024** Sep 9; 16(9):1190. (**IF= 4,9**).

During her doctoral studies, the doctoral student Boştiog Denisse-Iulia was a member of the implementation team of the following projects:

1. „Versatile molecular vectors with tailored carrying and actuating abilities, dedicated to gene and drug delivery in fight against cancer (TM-Vector), PN-III-P4-ID-PCE-2020-1523;
2. „Intelligent systems for cancer diagnosis and treatment (**IntelDots**)", PNRR-III-C9-2022 – I8;
3. „Multifunctional hybrid 3D architectures based on hollow GaN nano-micro-tetrapods for advanced application (**MultiPodGaN**)", PNRR-III-C9-2023-I8.

Research internships/mobilities carried out during doctoral studies:

1. Research internship at the Estonian University of Life Sciences, between 01.10.2023 - 31.10.2023 (0 months) within the project HORIZON-MSCA-2021-SE-01, *VOLATEVS* No 101086360;
2. The third edition of the SENSORFINT Spectroscopy Training School, held on July 3-5, 2024, at the Poznań University of Economics and Business.

Participation in international/national scientific events:

Oral communications

1. Multi-shell gold nanoparticles functionalized with methotrexate for targeted therapy of breast cancer*;* **D. I. Bostiog,** N. Simionescu, M. Pinteala*. 14th International Conference on Physics of Advanced Material (IPCAM-14)*, Dubrovnik, Croatia; 8-15 Septembrie **2022**;

2. Methotrexate-functionalized multi-shell gold nanoparticles for drug delivery applications; **D.I. Bostiog**, N. Simionescu, B. F. Craciun, M. Pinteala; *XXXIIIth edition of the International Congress of "Apollonia" University of Iasi. By promoting excellence, we prepare the future*, 2-5 Martie **2023**;

3. Innovations in Cancer Imaging and Therapy: The Role of Nanoparticles and Radiotracers; **D.I. Bostiog**, C. M. Uritu, C.M. Al-Matarneh, A. Coroaba, V. Ghizdovat, S. I. Filipiuc, B. I. Tamba, C. Stefanescu, V. Nastase, M. Pinteala. *12th International Symposium on Polyimides & High Performances Materials STEPI12*, Montpellier 4-7 Iunie **2023**.

Posters

1. Investigations on the layer by layer multi-shell gold nanoparticles functionalization for the development of effective non-viral gene vectors; **D. I. Bostiog**, B. F. Craciun, E. L. Ursu, Peptanariu, M. Pinteala. D. *7th International Congress on Biomaterials and Biosensors* (BIOMATSEN), Mugla, Turkey; 22-28 April **2022;**
2. Obtaining and comprehensive analysis of polymeric-based carbon nanostructures. **D.I. Bostiog**, B.F. Craciun, N. Simionescu, N.L. Marangoci, M. Pinteala; *Conferința Internațională 30th edition of PolyChar World Forum on Advanced Materials PolyChar'30*, Iași România, 11-13 septembrie **2024.**

Selective bibliographic resources

Balasubramanian, S.K. *et al.* (2010) 'Biodistribution of gold nanoparticles and gene expression changes in the liver and spleen after intravenous administration in rats', *Biomaterials*, 31(8), pp. 2034–2042. Available at: https://doi.org/10.1016/j.biomaterials.2009.11.079.

Bhamidipati, M. and Fabris, L. (2017) 'Multiparametric Assessment of Gold Nanoparticle Cytotoxicity in Cancerous and Healthy Cells: The Role of Size, Shape, and Surface Chemistry', *Bioconjugate Chemistry*, 28(2), pp. 449–460. Available at: https://doi.org/10.1021/acs.bioconjchem.6b00605.

Bostiog, D.I. *et al.* (2024) 'Multi-shell gold nanoparticles functionalized with methotrexate: a novel nanotherapeutic approach for improved antitumoral and antioxidant activity and enhanced biocompatibility', *Drug Delivery*, 31(1), p. Available at: https://doi.org/10.1080/10717544.2024.2388624.

Chen, G. *et al.* (2016) 'Peptide-Decorated Gold Nanoparticles as Functional Nano-Capping Agent of Mesoporous Silica Container for Targeting Drug Delivery', *ACS Applied Materials and Interfaces*, 8(18), pp. 11204–11209. Available at: https://doi.org/10.1021/acsami.6b02594.

Craciun, B.F. *et al.* (2023) 'Multilayer gold nanoparticles as non-viral vectors for targeting MCF-7 cancer cells', *Biomaterials Advances*, 144(October 2022), p. 213201. Available at: https://doi.org/10.1016/j.bioadv.2022.213201.

Ferreira, D. *et al.* (2020) 'Gold nanoparticles for vectorization of nucleic acids for cancer therapeutics', *Molecules*, 25(15). Available at: https://doi.org/10.3390/molecules25153489.

Medici, S. *et al.* (2021) 'Gold nanoparticles and cancer: Detection, diagnosis and therapy', *Seminars in Cancer Biology*, 76(May), pp. 27–37. Available at: https://doi.org/10.1016/j.semcancer.2021.06.017.

Niu, J. *et al.* (2017) 'Transdermal Gene Delivery by Functional Peptide-Conjugated Cationic Gold Nanoparticle Reverses the Progression and Metastasis of Cutaneous Melanoma', *ACS Applied Materials and Interfaces*, 9(11), pp. 9388–9401. Available at: https://doi.org/10.1021/acsami.6b16378.

Qiu, J.M. and DelVecchio Good, M.J. (2021) 'Making the best of multidisciplinary care for patients with malignant fungating wounds: A qualitative study of clinicians' narratives', *Palliative medicine*, 35(1), pp. 179–187. Available at: https://doi.org/10.1177/0269216320966498.

Singh, P. *et al.* (2024) 'Advanced Nanomaterials for Cancer Therapy: Gold, Silver, and Iron Oxide Nanoparticles in Oncological Applications', *Advanced Healthcare Materials*, 2403059. Available at: https://doi.org/10.1002/adhm.202403059.

Sudimack, J. and Lee, R.J. (2000) 'Targeted drug delivery via the folate receptor', *Advanced Drug Delivery Reviews*, 41(2), pp. 147–162. Available at: https://doi.org/10.1016/S0169-409X(99)00062-9.

Tran, N.T.T. *et al.* (2013) 'Synthesis of methotrexate-conjugated gold nanoparticles with enhanced cancer therapeutic effect', *Biochemical Engineering Journal*, 78, pp. 175–180. Available at: https://doi.org/10.1016/j.bej.2013.04.017.

Uboldi, C. *et al.* (2009) 'Gold nanoparticles induce cytotoxicity in the alveolar type-II cell lines A549 and NCIH441', *Particle and Fibre Toxicology*, 6, pp. 1–12. Available at: https://doi.org/10.1186/1743-8977-6-18.

Uritu, C.M. *et al.* (2024) 'Radiolabeled multi-layered coated gold nanoparticles, as potential biocompatible PET/SPECT tracers', *Journal of Materials Chemistry B* [Preprint]. Available at: https://doi.org/10.1039/d3tb02654j.

Vasiliu, T. *et al.* (2021) 'In silico study of PEI-PEG-squalene-dsDNA polyplex formation: The delicate role of the PEG length in the binding of PEI to DNA', *Biomaterials Science*, 9(19), pp. 6623–6640. Available at: https://doi.org/10.1039/d1bm00973g.